

Theoretical insights into thermal transport and structural stability mechanisms of triaxial compressed methane hydrate

Dong-Sheng Chen(陈东升), Ting-Ting Miao(缪婷婷), Cheng Chang(常程), Xu-Yang Guo(郭旭洋), Meng-Yan Guan(关梦言), and Zhong-Li Ji(姬忠礼)

Citation: Chin. Phys. B, 2024, 33 (**9**): 096501. DOI: 10.1088/1674-1056/ad57ae
Journal homepage: http://cpb.iphy.ac.cn; http://iopscience.iop.org/cpb

What follows is a list of articles you may be interested in

Wide frequency phonons manipulation in Si nanowire by introducing nanopillars and nanoparticles

Yatao Li(李亚涛), Yingguang Liu(刘英光), Xin Li(李鑫), Hengxuan Li(李亨宣), Zhixiang Wang(王志香), and Jiuyi Zhang(张久意)
Chin. Phys. B, 2024, 33 (**4**): 046502. DOI: 10.1088/1674-1056/ad0290

Molecular dynamics study on the dependence of thermal conductivity on size and strain in GaN nanofilms

Ying Tang(唐莹), Junkun Liu(刘俊坤), Zihao Yu(于子皓), Ligang Sun(孙李刚), and Linli Zhu(朱林利)
Chin. Phys. B, 2023, 32 (**6**): 066502. DOI: 10.1088/1674-1056/acbf26

Magneto-volume effect in Fe_nTi_{13-n} clusters during thermal expansion

Jian Huang(黄建), Yanyan Jiang(蒋妍彦), Zhichao Li(李志超), Di Zhang(张迪), Junping Qian(钱俊平), and Hui Li(李辉)
Chin. Phys. B, 2023, 32 (**4**): 046501. DOI: 10.1088/1674-1056/acaf2e

Alkyl group functionalization-induced phonon thermal conductivity attenuation in graphene nanoribbons

Caiyun Wang(王彩云), Shuang Lu(鲁爽), Xiaodong Yu(于晓东), Haipeng Li(李海鹏)
Chin. Phys. B, 2019, 28 (**1**): 016501. DOI: 10.1088/1674-1056/28/1/016501

Thermal transport in phosphorene and phosphorene-based materials: A review on numerical studies

Yang Hong(洪扬), Jingchao Zhang(张景超), Xiao Cheng Zeng(曾晓成)
Chin. Phys. B, 2018, 27 (**3**): 036501. DOI: 10.1088/1674-1056/27/3/036501

Theoretical insights into thermal transport and structural stability mechanisms of triaxial compressed methane hydrate

Dong-Sheng Chen(陈东升)[1], Ting-Ting Miao(缪婷婷)[1,†], Cheng Chang(常程)[1], Xu-Yang Guo(郭旭洋)[2], Meng-Yan Guan(关梦言)[1], and Zhong-Li Ji(姬忠礼)[1]

[1] *Beijing Key Laboratory of Process Fluid Filtration and Separation, College of Mechanical and Transportation Engineering, China University of Petroleum-Beijing, Beijing* 102249, *China*

[2] *State Key Laboratory of Petroleum Resources and Prospecting, China University of Petroleum-Beijing, Beijing* 102249, *China*

(Received 23 April 2024; revised manuscript received 27 May 2024; accepted manuscript online 13 June 2024)

The heat transfer and stability of methane hydrate in reservoirs have a direct impact on the drilling and production efficiency of hydrate resources, especially in complex stress environments caused by formation subsidence. In this study, we investigated the thermal transport and structural stability of methane hydrate under triaxial compression using molecular dynamics simulations. The results suggest that the thermal conductivity of methane hydrate increases with increasing compression strain. Two phonon transport mechanisms were identified as factors enhancing thermal conductivity. At low compressive strains, a low-frequency phonon transport channel was established due to the overlap of phonon vibration peaks between methane and water molecules. At high compressive strains, the filling of larger phonon bandgaps facilitated the opening of more phonon transport channels. Additionally, we found that a strain of −0.04 is a watershed point, where methane hydrate transitions from stable to unstable. Furthermore, a strain of −0.06 marks the threshold at which the diffusion capacities of methane and water molecules are at their peaks. At a higher strain of −0.08, the increased volume compression reduces the available space, limiting the diffusion ability of water and methane molecules within the hydrate. The synergistic effect of the strong diffusion ability and high probability of collision between atoms increases the thermal conductivity of hydrates during the unstable period compared to the stable period. Our findings offer valuable theoretical insights into the thermal conductivity and stability of methane hydrates in reservoir stress environments.

Keywords: methane hydrate, molecular dynamics, thermal transport, triaxial compression, structural stability

PACS: 65.40.–b, 64.60.–i, 91.50.Hc, 31.15.xv **DOI:** 10.1088/1674-1056/ad57ae

1. Introduction

Natural gas hydrates (NGHs) are nonstoichiometric crystalline compounds characterized by cage structures formed by water (host) molecules enclosing small gas (guest) molecules under low-temperature and high-pressure conditions.[1] There are three main types of hydrates: structure I (sI), structure II (sII), and structure H (sH). The sI-type hydrates are the most common in nature,[1] with most of their guest molecules being methane.[2] Additionally, hydrate resources, which are commonly found in marine sediments and permafrost regions,[3] contain approximately twice the energy content of fossil fuels.[4] In particular, 1 m^3 of hydrate can produce approximately 164 m^3 of natural gas and 0.8 m^3 of water.[5] Therefore, NGHs are a potential clean energy source that is expected to alleviate the current energy crisis. However, a series of challenges hinder the commercial development of NGH.[6] For instance, the dissociation of hydrates during drilling and production can lead to geological disasters, such as formation subsidence and submarine landslides, creating a complex stress environment in the reservoir.[7] Moreover, the development of NGH resources involves a series of heat and mass transfer processes. To accurately assess future hydrate development, it is essential to understand the heat transfer and structural stability of hydrates under stress environments.

Recently, the thermal transport properties of hydrate-bearing sediments (HBSs) have garnered significant research interest. For instance, Chen *et al.*[8] found that the effective thermal conductivity increased with an increase in hydrate saturation, reaching a maximum value in the range of 25%–36% hydrate saturation using a steady-state method. Guo *et al.*[9] investigated the thermal conductivity of methane hydrate in porous media using molecular dynamics (MD) simulations, and their results indicated that the methane hydrate-porous media system exhibits the characteristics of a glass body. As the pore size of the porous medium decreases, the thermal conductivity of the system gradually increases. Moreover, the thermal conductivity of HBS under stress environments has garnered attention. For example, Cortes *et al.*[10] measured the thermal conductivity of tetrahydrofuran HBS at different vertical effective stresses. They discovered that a tenfold increase in the vertical effective stress resulted in an enhancement of the thermal conductivity by more than twofold. Kim and Yun[11] measured the thermal conductivity of methane HBS under a vertical effective stress of 1.52 MPa using the transient plane source method. However, their study focused on the effect of hydrate saturation and did not examine the

†Corresponding author. E-mail: mting@cup.edu.cn

© 2024 Chinese Physical Society and IOP Publishing Ltd

impact of stress. Morita *et al.*[12] studied the thermal conductivity of HBS under vertical stress using the hot-disk transient method. Their results suggested that the thermal conductivity enhanced from 1.53 $W{\cdot}m^{-1}{\cdot}K^{-1}$ to 1.75 $W{\cdot}m^{-1}{\cdot}K^{-1}$ as stress increased from 0.06 MPa to 2.36 MPa. Because of limitations in experimental technology and the harsh conditions required for hydrates, measuring the thermal conductivity of hydrates under stress environments is particularly challenging. Lei *et al.*[13] developed a new analytical model for the effective thermal conductivity of HBS, elucidating the influence mechanism of parameters, such as effective stress, on the effective thermal conductivity. However, prior research has primarily focused on measuring the effective thermal conductivity of HBS under stress. To the best of our knowledge, only a few studies have investigated the impact of stress on the thermal conductivity of pure hydrates. As a substitute, MD simulations offer an effective means of investigating the thermal properties of pure hydrates under stress conditions. For instance, Xu *et al.*[14] studied the effect of triaxial strain from -0.04 to 0.06 on the thermal conductivity of pure methane hydrate using MD simulations. Their results indicated that the thermal conductivity of methane hydrate initially decreased, followed by a sudden increase as the strain transitioned from compressive to tensile. They attributed this change to the softening and hardening of the phonons. In our previous study,[15] we investigated phonon transport mechanisms in methane hydrate under various uniaxial compressive strains using MD simulations. Our results suggest that the thermal conductivity initially increased and then decreased during uniaxial compression, reaching its maximum value at a strain of -0.04. It was ultimately discovered that the overlap of phonon vibrations between methane and water molecules led to the opening of phonon transport channels, thereby enhancing heat transport in methane hydrates. Our research fills a gap in the study of phonon transport mechanisms under uniaxial compression. Currently, there is still a lack of research on the thermal transport mechanisms of methane hydrate under both uniaxial and triaxial strains. In particular, it remains unclear whether the phonon transport mechanisms of methane hydrate under higher triaxial compressive strains are consistent with those under lower compressive strains.

Additionally, the structural stability of hydrates under stress environments has garnered increasing attention due to its crucial role in the exploitation of hydrates. For example, Shu *et al.*[16] demonstrated that sI-type methane hydrate transformed into the sII type at 120 MPa and subsequently into the sH type at 600 MPa. Moreover, methane hydrate decomposes at pressures greater than 3.0 GPa, resulting in the formation of methane and ice with an orientationally disordered structure. Cao *et al.*[17] investigated the mechanical properties of methane hydrates under mechanical loading using MD simulations. Their results suggest that the engineering strain rate, temperature, and guest molecule occupancy in large cages significantly impact the mechanical strength and failure strain of methane hydrates. Moreover, using MD simulations, Lin *et al.*[18] suggested that the mechanical properties of methane hydrate are influenced by both the density and type of water vacancies. Carbon dioxide (CO_2) hydrate also demonstrates similar mechanical properties.[19] Furthermore, Zhang *et al.*[20] explored the mechanical properties of CO_2 hydrates with varying occupancy rates and occupancy distributions. They found that voids in large cages significantly affected the overall mechanical stability compared to those in small cages. Wang *et al.*[21] investigated the structural stability of clathrate hydrates encapsulating fluorinated methane derivatives under mechanical loading using MD simulations. They found that clathrate hydrates encapsulating nonpolar fluorinated methane exhibited superior mechanical properties compared to those encapsulated by polar fluorinated methane. In addition, using MD simulations, Song *et al.*[22] explored the diffusion mechanisms of H_2 in a new phase of clathrate hydrates. They demonstrated that the diffusion of H_2 molecules was governed primarily by a hopping mechanism. The aforementioned studies have demonstrated that factors, such as pressure, temperature, occupancy rate, polarity, and guest molecule type, significantly influence the mechanical stability of hydrates. Nevertheless, the mechanisms underlying the stability and destabilization of methane hydrates during compression remain unclear.

In this study, we investigated the phonon transport and structural stability of methane hydrates under triaxial compressive strain using MD simulations. The subsequent structure of this paper is organized as follows: Section 2 focuses on the establishment of a methane hydrate model and introduces the simulation details. In Section 3, we present an in-depth discussion of our findings. The phonon density of states (PDOS) and spectral energy density (SED) were employed to elucidate the thermal conduction mechanisms of the hydrates under various compressive strains. Then, the structural stability of methane hydrate was analyzed using various methods, including stress–strain curves, structural factors, visualizations of residual hydrate structures, and four-body angular order parameters. Subsequently, mean square displacements (MSDs) and diffusion coefficients were employed to assess the stability of the hydrate structures under compressive strain. In Section 4, we provide a comprehensive summary of our study along with a forward-looking outlook.

2. Simulation methods

2.1. Model configurations

In this study, the sI-type methane hydrate was selected as the simulation model because of its abundance in nature.[23] It comprises two polyhedral cages, designated as 5^{12} (pentag-

onal dodecahedron) and $5^{12}6^2$ (tetradecahedron with 12 pentagons and two hexagons) cages. The lattice constant of this model is 1.2 nm. Its unit cell contains 46 water molecules and eight methane molecules, constituting two 5^{12} and six $5^{12}6^2$ cages. Herein, the initial atomic coordinates in the sI-type methane hydrate were derived from the x-ray diffraction experimental data.[24] As depicted in Fig. 1, an initial bulk model of sI-type methane hydrate was constructed using the Moltemplate[25] package by expanding the unit cell three times in the x, y, and z directions. The dimension of the bulk methane hydrate is 3.6 nm×3.6 nm×3.6 nm. Perspective (Fig. 1(a)) and front (Fig. 1(b)) views of the methane hydrate block were rendered using the Python interface in OVITO.[26] The yellow spheres represent methane (CH_4) molecules, the red spheres represent oxygen (O) atoms in water, and the white spheres denote hydrogen (H) atoms in water. The cage occupancy rate of the constructed methane hydrate model is 100%.

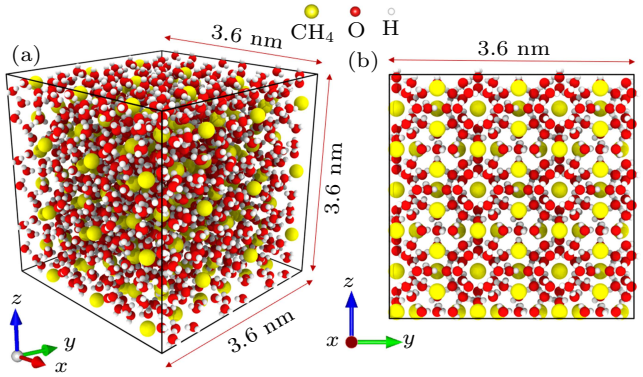


Fig. 1. (a) Perspective and (b) front views of the initial molecular model of the sI-type methane hydrate. The yellow spheres represent methane (CH_4) molecules, the red spheres represent oxygen (O) atoms in water molecules, and the white spheres denote hydrogen (H) atoms in water molecules.

2.2. Force fields

This study employed the TIP4P/Ice[27] model and the optimized potentials for liquid simulations united atom (OPLS-UA)[28] force field to describe the water and methane molecules in methane hydrate, respectively. TIP4P/Ice water is a rigid molecule, meaning its bond length (0.9572 Å) and angle (104.52°) are held constant. In addition, this water model is a four-point model that includes three real atoms and a massless virtual charge site M. The distance (d_{OM}) between the O atom and virtual site M in a water molecule was fixed at 0.1577 Å. The H atoms in this water model adhere to the Bernal–Fowler rules[29] and are frequently employed to investigate the various properties of solid water, such as ice and hydrates. Additionally, the OPLS-UA methane molecule is a single-point model, and its predictions of various methane properties generally align with experimental data.[28] Previous studies have successfully employed these two force fields to investigate the thermal transport and stability mechanisms of methane hydrates.[14,15] The interaction potential ($U(r_{ij})$) encompasses both van der Waals and electrostatic interactions and can be defined as follows:

$$U(r_{ij}) = 4\varepsilon_e\left[\left(\frac{\sigma}{r_{ij}}\right)^{12} - \left(\frac{\sigma}{r_{ij}}\right)^{6}\right] + \frac{q_i q_j}{4\pi\varepsilon_0 r_{ij}}. \quad (1)$$

The first term on the right-hand side of Eq. (1) represents the Lennard–Jones (LJ) potential; ε_e and σ represent the energy and distance parameters between the atoms (or molecules), respectively; and r_{ij} represents the distance between atoms (or molecules) i and j. The energy ($\varepsilon_{e,ij}$) and distance (σ_{ij}) parameters between different atoms (or molecules) adhere to the Lorentz–Berthelot rules, which are defined as follows:

$$\varepsilon_{e,ij} = \sqrt{\varepsilon_{e,ii}\varepsilon_{e,jj}}, \quad (2)$$

$$\sigma_{ij} = \frac{1}{2}(\sigma_{ii} + \sigma_{jj}). \quad (3)$$

Additionally, the second term on the right-hand side of Eq. (1) represents the Coulomb potential; q_i and q_j are the charges of atoms (or molecules) i and j, respectively; and ε_0 is the permittivity of the vacuum. The specific force field parameter values for water and methane molecules are listed in Table 1.

Table 1. Force field parameters of methane hydrate.

Species	ε_e (kcal/mol)	σ (Å)	q (e)
Oxygen (O)[a)]	0.21084	3.1668	–1.1794
Hydrogen (H)[a)]	0.0000	0.0000	0.5897
Methane (CH_4)[b)]	0.29400	3.7300	0.0000

[a)]Ref. [27], [b)]Ref. [28].

2.3. Simulation details

All MD simulations in this study were carried out using the Large-scale Atomic/Molecular Massively Parallel Simulator (LAMMPS).[30] Periodic boundary conditions were applied in all directions throughout the simulation. The velocity Verlet method was employed to iteratively solve Newton's equations of motion. The time step was set to 1.0 fs. The cutoff distances for both the van der Waals and Coulomb interactions were set to 1.0 nm. Moreover, we employed the particle–particle–particle–meth (PPPM) algorithm[31] to calculate long-range electrostatic interactions. The SHAKE algorithm[32] was used to constrain the water molecules. Before the formal simulation, the initial model underwent energy minimization using the steepest descent method to eliminate the interatomic residual stress. The system was then relaxed in the isothermal–isobaric (NPT) ensemble for 1.0 ns to maintain the temperature at 287 K and a pressure of 14 MPa. Here, we employed the Nosé–Hoover thermostat and barostat[33] to control temperature and pressure, respectively. The temperature and pressure conditions used in this study represent those found in the hydrate reservoir in the South China Sea.[34] Subsequently, a triaxial compression simulation was conducted under the canonical (NVT) ensemble at a temperature of 287 K and an engineering strain rate of 10^7 s^{-1}. This engineering

strain rate has been deemed suitable for the mechanical characteristics of methane hydrates.[14,15] During the simulated compression, the triaxial strain (ε) of methane hydrate at time t can be defined as follows:

$$\varepsilon = \frac{L_t - L_0}{L_0}, \tag{4}$$

where L_t and L_0 represent the simulation box in all directions at times t and 0, respectively. Additionally, the triaxial stress was calculated by the formula

$$S = \frac{Nk_{\mathrm{B}}T}{V} + \frac{1}{Vd}\sum_{i=1}^{N'} \boldsymbol{r}_i \cdot \boldsymbol{f}_i, \tag{5}$$

where N represents the number of atoms in the methane hydrate system, k_{B} represents the Boltzmann constant, T denotes the temperature of the simulation system, and V is the volume. In addition, d is the dimensionality of the simulation system, and in this study, the value of d was 3; $\boldsymbol{r}_i$ and $\boldsymbol{f}_i$ represent the position and force vectors of atom i, respectively. Thus, the stress–strain curve of methane hydrate can be obtained using Eqs. (4) and (5). To further access the thermal transport properties of methane hydrate under different strains, we preserved the hydrate structures at strains of 0.00, −0.02, −0.04, −0.06, and −0.08 during the compression process.

Furthermore, we performed equilibrium MD (EMD) simulations to compute the thermal conductivity of deformed methane hydrate. First, a 1.0 ns canonical ensemble simulation was performed to stabilize the temperature of the deformed methane hydrate at 287 K. Then, a 1.5 ns microcanonical (NVE) ensemble was carried out to record the heat flux. Finally, the thermal conductivity of methane hydrate was determined by integrating the heat flux autocorrelation (HFAC) function according to the Green–Kubo formula[35]

$$\kappa = \frac{V}{3k_{\mathrm{B}}T^2}\int_0^{\infty} \langle \boldsymbol{J}(0)\boldsymbol{J}(t)\rangle \mathrm{d}t, \tag{6}$$

where $\boldsymbol{J}(0)$ and $\boldsymbol{J}(t)$ represent the heat flux vector at times 0 and t, respectively. The angle bracket represents ensemble averages. Herein, the thermal conductivity of the deformed methane hydrate was averaged by conducting 50 independent EMD simulations.

3. Results and discussion

3.1. Thermal transport mechanisms

In this section, we focus on the thermal conductivity of methane hydrate under triaxial strains of 0.00, −0.02, −0.04, −0.06, and −0.08. A correlation time of 10 ps was selected and verified as appropriate in our previous study.[15] As depicted in Fig. 2(a), the HFAC function converged within 1.0 ps. Furthermore, the running thermal conductivity was calculated by integrating the HFAC function using the Green–Kubo method, as illustrated in Fig. 2(b). After 2.0 ps, the thermal conductivity of the methane hydrate converged, and the shaded area indicates the error margin. As shown in Fig. 2(c), the thermal conductivities of methane hydrate under different triaxial compressive strains were obtained using Eq. (6). The results showed that the thermal conductivity of methane hydrate increases with increasing compressive strain. Moreover, the rate of increase in the thermal conductivity was slower in the strain range of 0.00 to −0.04 compared to the range of −0.04 to −0.08. To quantitatively analyze the trend of the thermal conductivity change, the thermal conductivity growth rates in the slow and fast stages were obtained by fitting the thermal conductivity of methane hydrate with different strains. It was found that the thermal conductivity growth rate at a strain of −0.04 to −0.08 was around 5.86, which was approximately four times the growth rate (1.46) of the thermal conductivity of methane hydrate at a strain of 0 to −0.04. This trend in thermal conductivity change differs from our previous results on uniaxial compression.[15] Specifically, the uniaxial compressions caused the phonon vibration modes of methane and water molecules in the hydrate to overlap, eliminating the gap at a strain of −0.04, resulting in a peak thermal conductivity. Furthermore, the gap reappeared when the compressive strain exceeded 0.04, causing a decrease in thermal conductivity. However, in this study, triaxial compression resulted in a monotonic increase in the thermal conductivity of the methane hydrate. We believe that there are additional mechanisms that

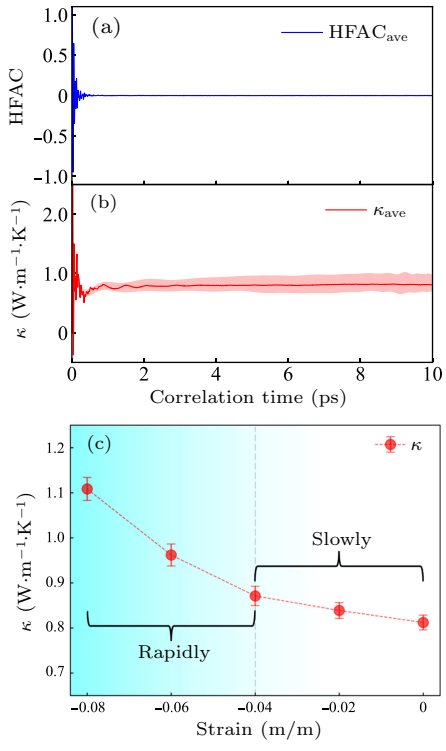


Fig. 2. (a) Normalized average HFAC function (HFAC$_{ave}$) and (b) running thermal conductivity of methane hydrate as a function of correlation time when the strain is 0.00. (c) Thermal conductivity of methane hydrate at strains of 0.00, −0.02, −0.04, −0.06, and −0.08.

influence the heat transfer properties of methane hydrate under triaxial compressive strains. It is preliminarily inferred that the instability of local cages caused by methane hydrate deformation may contribute to the differences in the thermal conductivity observed between uniaxial and triaxial compression.

To investigate the underlying mechanism for the enhancement of thermal conductivity due to compressive strain, we calculated PDOS ($P(\omega)$) for methane hydrate, water molecules in hydrate, and methane molecules in hydrate. $P(\omega)$ can be obtained by integrating the autocorrelation of atomic velocities[36]

$$P(\omega) = \int_0^{\tau_0} \frac{v(0)\cdot v(t)}{v(0)\cdot v(0)} \exp(-2\pi \mathrm{i}\omega t)\,\mathrm{d}t, \tag{7}$$

where τ_0 represents the simulation time, $v(0)$ is the initial velocity of atoms, and $v(t)$ is the velocity of atoms at time t.

PDOS represents the vibration modes of phonons at various frequencies. As depicted in Fig. 3, we compared the PDOS of methane hydrate, water in hydrate, and methane in hydrate at strains of 0.00, −0.04, and −0.08. As shown in Fig. 3(a), an increase in strain led to a monotonic decrease in the first peak of the PDOS for methane hydrate. In particular, the first peak positions at low frequencies (0–5 THz) shifted leftward as strain varied from 0.00 to −0.04. Conversely, when strain varied from −0.04 to −0.08, the main peak positions shifted rightward. A similar phenomenon occurred in the high-frequency region (15–20 THz), but the direction of the peak shift was opposite to that observed at low frequencies. Moreover, a right shift was observed for the peak position in the midfrequency region, but the peak largely disappeared at a strain of −0.08. The result suggests that a strain of −0.04 represents a critical point for phonon transport in triaxial compression, similar to that observed in uniaxial compression.[15] Interestingly, the three main peaks became flatter, and the gaps between the peaks were nearly filled when the triaxial compressive strain exceeded 0.04. This observation differs from that of uniaxial compression. This may be one of the primary reasons for the monotonic increase in the thermal conductivity. Additionally, as illustrated in Figs. 3(a) and 3(b), the PDOS of methane hydrate and water molecules were nearly identical, with only slight variations due to methane at low frequencies. This suggests that the primary factor influencing the thermal conductivity of hydrates is the water cage structure within the hydrates.

To observe the effect of strains on the phonon vibration in methane molecules, we compared the PDOS of methane molecules at strains of 0.00, −0.04, and −0.08, as illustrated in Fig. 3(c). As the compressive strain increased, the peak value of the PDOS of the methane molecules decreased steadily, and the peak position shifted gradually to the right. This led to the phonons in methane and water molecules gradually overlapping in vibration at low strains (0.00 to −0.04), creating a dominant phonon transport channel at a strain of −0.04. With further compression, the co-directional vibrations of methane and water molecules disrupted the gap and enhanced phonon transport. From the preceding analysis, we identified two distinct mechanisms for enhancing the thermal conductivity. On the one hand, similar to uniaxial compression, the gap between water and methane molecules in the low frequency (0–5 THz) disappeared in Fig. 3(a) during the strain range from 0.00 to −0.04. This opened up the low-frequency phonon transport channel that led to an increase in thermal conductivity. On the other hand, the low-frequency vibration peaks of methane and water molecules both co-shifted to higher frequencies during the strain range from −0.04 to −0.08, whereas the high-frequency (15–25 THz) phonon vibrations of water molecules gradually moved to lower frequencies. This filled the two larger gaps between the three main peaks, thereby opening more phonon transport channels.

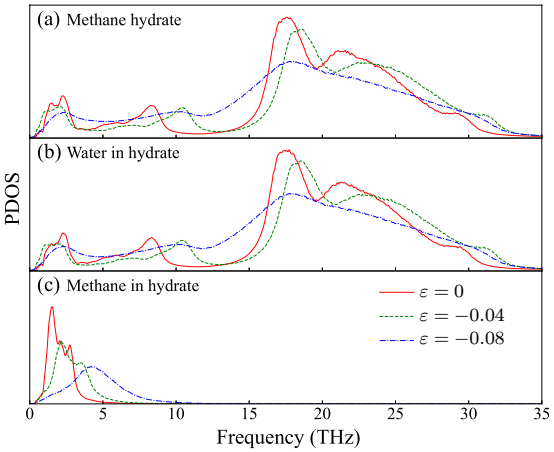


Fig. 3. PDOS of (a) methane hydrate, (b) water in hydrate, and (c) methane in hydrate at strains of 0.00, −0.04, and −0.08.

To further investigate phonon transport mechanisms, the normalized SED, represented as $\Phi(\boldsymbol{k},\omega)$, is a function of both the wave vector ($\boldsymbol{k}$) and frequency (ω). SED can be calculated using the following equation:[36–38]

$$\Phi(\boldsymbol{k},\omega) = \frac{1}{4\pi\tau_0 N_{\mathrm{T}}} \sum_{\alpha}\sum_{b}^{B} m_b \left| \int_0^{\tau_0} \sum_{n_{x,y,z}}^{N_{\mathrm{T}}} u_\alpha \begin{pmatrix} n_{x,y,z} \\ b \end{pmatrix}; t \right) \times \exp\left[\mathrm{i}\boldsymbol{k}\cdot\boldsymbol{r} \begin{pmatrix} n_{x,y,z} \\ 0 \end{pmatrix} - \mathrm{i}\omega t \right] \mathrm{d}t \right|^2, \tag{8}$$

where N_{T} represents the total number of unit cells in hydrate, and n_{xyz} is the index of unit cells. B represents the total number of atoms in the unit cell, m_b denotes the mass of atom b, u_α represents the velocity in the α direction, and r is the equilibrium position vector of atoms.

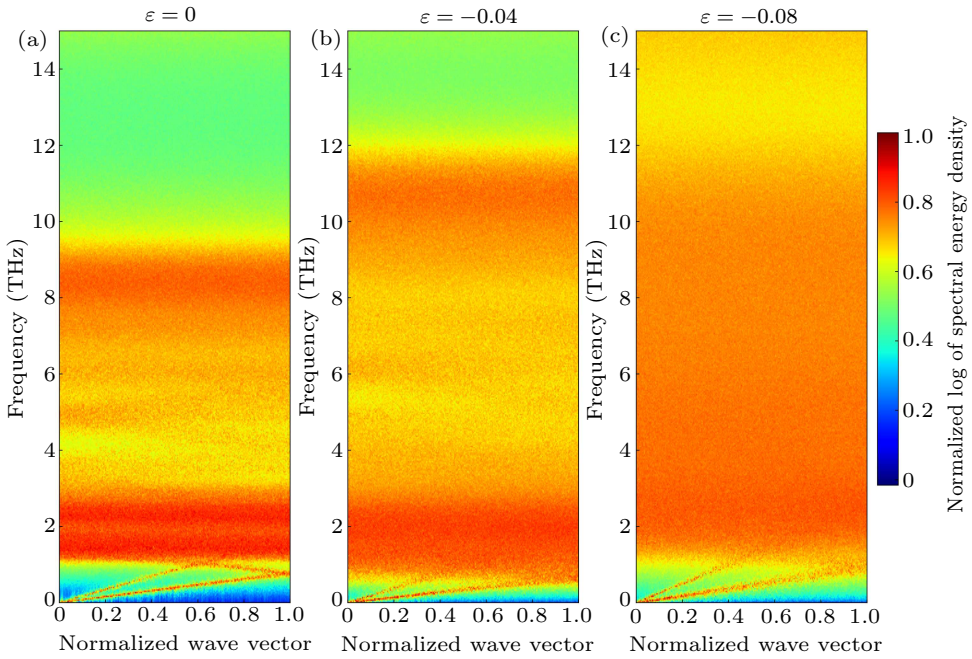


Fig. 4. Normalized SED of methane hydrate at strains of (a) 0.00, (b) −0.04, and (c) −0.08 at 0–15 THz.

In general, phonon modes in the low-frequency range contribute more to thermal conductivity.[39] As illustrated in Fig. 4, we plotted the normalized SED of methane hydrate at strains of 0.00, −0.04, and −0.08 using Eq. (8) at 0–15 THz. The results suggest that the spectral energies under strains of −0.04 and −0.08 are lower than those under a strain of 0.00. The acoustic phonon branches of methane hydrate exhibited softening and broadening at a strain of −0.04 (Fig. 4(b)) compared to a strain of 0.00 (Fig. 4(a)). This implies a decrease in the phonon group velocity and relaxation time of the acoustic branch, which could lead to a reduction in thermal conductivity. Interestingly, we noticed that the frequency distribution range of the high SED extended to both the higher and lower frequencies (Fig. 4(b)). This expansion phenomenon not only broadened the frequency range of phonon transmission but also enhanced the energy flux of low-frequency phonons, which played a dominant role in thermal transport. The PDOS results in Fig. 3 also confirm that this expansion of phonon vibration fills the bandgap and broadens the phonon transport channels. The contributions of these mechanisms to thermal conductivity may exceed the impact of strains on the acoustic phonon branches. Consequently, the thermal conductivity of methane hydrate increased gradually from 0.00 to −0.04 strain. As illustrated in Fig. 3(c), the frequency range of high SED expanded further at a strain of −0.08 compared to low compressive strains. In particular, the rehardening of the acoustic phonon branches contributed to enhanced phonon transport. Finally, the competition of multiple mechanisms produced the thermal conductivity results (Fig. 2(c)). Specifically, the thermal conductivity increased slowly at low strains (0.00 to −0.04) and accelerated significantly at high strains (−0.04 to −0.08).

3.2. Structural stability

3.2.1. Structural properties

The thermal conductivity results revealed differences in the thermal transport mechanism before and after a strain of −0.04. The stability mechanism of hydrates under compressive strain may play a crucial role in influencing thermal transport. As illustrated in Fig. 5(a), the stress–strain curve of methane hydrate during the compression process was obtained to understand the effect of structural stability using Eqs. (4) and (5). Observations revealed that stresses in all three directions followed a consistent trend, with stress increasing alongside the compressive strain. Notably, the stress curves initially plateaued before slowly increasing after a strain of −0.04. This result contrasts with the linear increase in stress during uniaxial strain,[15] suggesting that the structure of methane hydrate may undergo significant changes after a strain of −0.04.

To explore the influence of triaxial strains on the structural information of methane hydrate, we calculated the static structural factors ($S(k)$) using the Debye scattering equation[40,41]

$$S(\boldsymbol{k}) = \frac{1}{N}\sum_{i=0}^{N}\sum_{j=0}^{N}\mathrm{sinc}\,(\boldsymbol{k}\boldsymbol{r}_{ij}), \tag{9}$$

where $\boldsymbol{k}$ is the wave vector, the minimum valid value of $\boldsymbol{k}$ is $4\pi/L$, and L represents the minimum side length of the system box. N represents the number of particles. The sinc function is defined as $\sin(\boldsymbol{k}\boldsymbol{r}_{ij})/(\boldsymbol{k}\boldsymbol{r}_{ij})$, where $\boldsymbol{r}_{ij}$ represents the position vector between atoms i and j. $S(\boldsymbol{k})$ is an essential parameter for describing the local structural information of materials as

it reflects the structure of a system in reciprocal space. Moreover, the height of the first peak in $S(\boldsymbol{k})$ is a key parameter that characterizes the liquid–solid phase transition. As depicted in Fig. 5(b), the first peak value of $S(\boldsymbol{k})$ gradually decreased with increasing compressive strain. This suggests that methane hydrate transitions from a state of long-range order to a disordered state under strain. However, even at a strain of −0.08, the peaks persisted, indicating that methane hydrate retained some crystalline characteristics at this strain level.

To visually characterize the stability of the water cages within methane hydrate, we identified residual hydrate cages under various strains using a self-program code. The residual hydrate structures were visualized using the VMD software.[42] As shown in Fig. 5(c), red dynamic bonds represent water cages, yellow spheres denote methane molecules, and blue dots symbolize decomposed water molecules. The hydrate cage structure was progressively compressed as compressive strain increased. When the compressive strain exceeds 0.04, the local hydrate cage collapses. Notably, almost no intact water cages remained in the hydrate at a strain of −0.08. Nevertheless, some residual cages persisted and retained solid-phase characteristics. To further examine the stability of the methane molecules in the residual hydrate cage, we calculated the two-dimensional (2D) number density distribution of the methane molecules, as depicted in Fig. 5(d). Under strains of 0.00, −0.02, and −0.04, there was minimal escape of methane molecules, which was closely associated with the retention of more intact hydrate cages. However, methane molecules within some hydrate cages underwent mass transfer at strains of −0.06 and −0.08. Interestingly, according to Figs. 5(c) and 5(d), some residual cages effectively prevented methane molecules from escaping. This suggests that, despite the deformation and breakdown of some hydrate cages, methane–water molecule interactions and the network of hydrogen bonds may continue to prevent methane molecules from escaping.

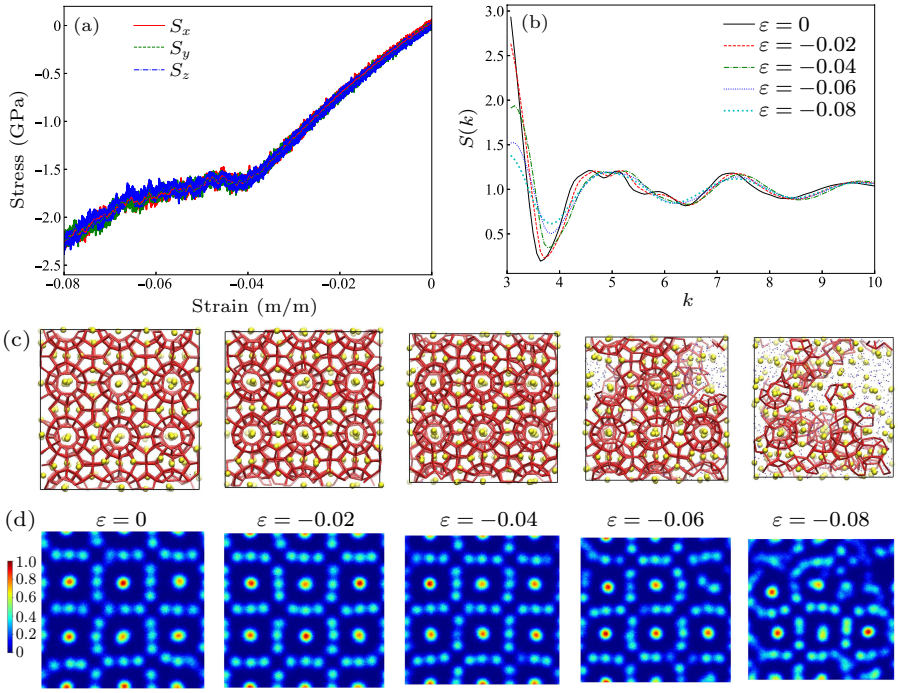


Fig. 5. (a) Stress–strain curve of methane hydrate under triaxial compression. (b) Structural factor ($S(\boldsymbol{k})$) of methane hydrate at strains of 0.00, −0.02, −0.04, −0.06, and −0.08. (c) Residual methane hydrate cage structure and (d) 2D number density distribution of methane molecules in hydrate under different compressive strains.

To further analyze the effect of strain on the structural stability of methane hydrate, the radial distribution functions (RDFs, $g_{\alpha\beta}(r)$) under various strains were calculated as follows:

$$g_{\alpha\beta}(r) = \frac{V}{N_\alpha N_\beta}\left(\sum_{i=1}^{N_\alpha}\frac{n_{i\beta}(r)}{4\pi r^2 \Delta r}\right), \tag{10}$$

where V is the volume of the simulation system. N_α is the number of atoms α, and N_β is the number of atoms β. The $n_{i\beta}(r)$ function represents the number of β atoms at distance r from the ith α atom. In contrast to structural factors based on reciprocal space, $g_{\alpha\beta}(r)$ provides the probability of a particle at distance r from a reference particle in direct space. In crystalline materials, $g_{\alpha\beta}(r)$ displays distinct peaks that correspond to the periodic arrangement of particles, demonstrating the presence of a long-range order. To quantify the number of neighboring atoms around a specific atom or molecule in methane hydrate, the coordination number ($CN_{\alpha\beta}(r)$) can be calculated by integrating $g_{\alpha\beta}(r)$

$$CN_{\alpha\beta}(r) = 4\pi\rho\int_{r_0}^{r_1} r^2 g_{\alpha\beta}(r)\,\mathrm{d}r, \tag{11}$$

where ρ represents the local number density.

As illustrated in Fig. 6, $g_{\alpha\beta}(r)$ and $CN_{\alpha\beta}(r)$ of the oxygen atom (O–O) pairs, methane molecule and oxygen atom (M–O) pairs, and methane molecule (M–M) pairs were calculated at different strains. In Fig. 6(a), the first peak of the RDF of the O–O pairs increased when the strain ranged from 0.00 to −0.04, and the first peak valley position shifted to the left. This suggests an increase in the local density of water at low strains. However, the first peak decreased when the strain ranged from −0.04 to −0.08, and the first peak valley position shifted to the right. This means that the arrangement of water molecules increasingly resembled a liquid phase compared to other strains at strains of −0.06 and −0.08. This amorphous structure of methane hydrate under high strain may lead to an increase in inelastic phonon interactions,[43] thereby enhancing thermal conductivity. The increased $CN_{\mathrm{O-O}}(r)$ shown in Fig. 6(d) demonstrates that compressive strain causes oxygen atoms in the hydrate to aggregate continuously. Additionally, as depicted in Fig. 6(b), the first two RDF peaks of the M–O pair increased monotonically with the compressive strain, and the peak positions shifted steadily to the left. The number of water molecules surrounding the methane molecules increased with the strain, as shown in Fig. 6(e). This suggests that an increased strain increases the likelihood of contact between the methane and water molecules. Additionally, the trend of the RDF peak of the M–M pair mirrors that of the O–O pair, whereas the change in the peak position resembles that of the M–O pair. More intriguingly, new peaks emerged around 3.6 Å at strains of −0.04 and −0.08 in Fig. 6(c), suggesting the formation of methane bubbles. Additionally, the coordination number that resulted for the M–M pair was similar to those for the O–O and M–O pairs. The number of atoms or molecules aggregating around each other also increased as the strain increased.

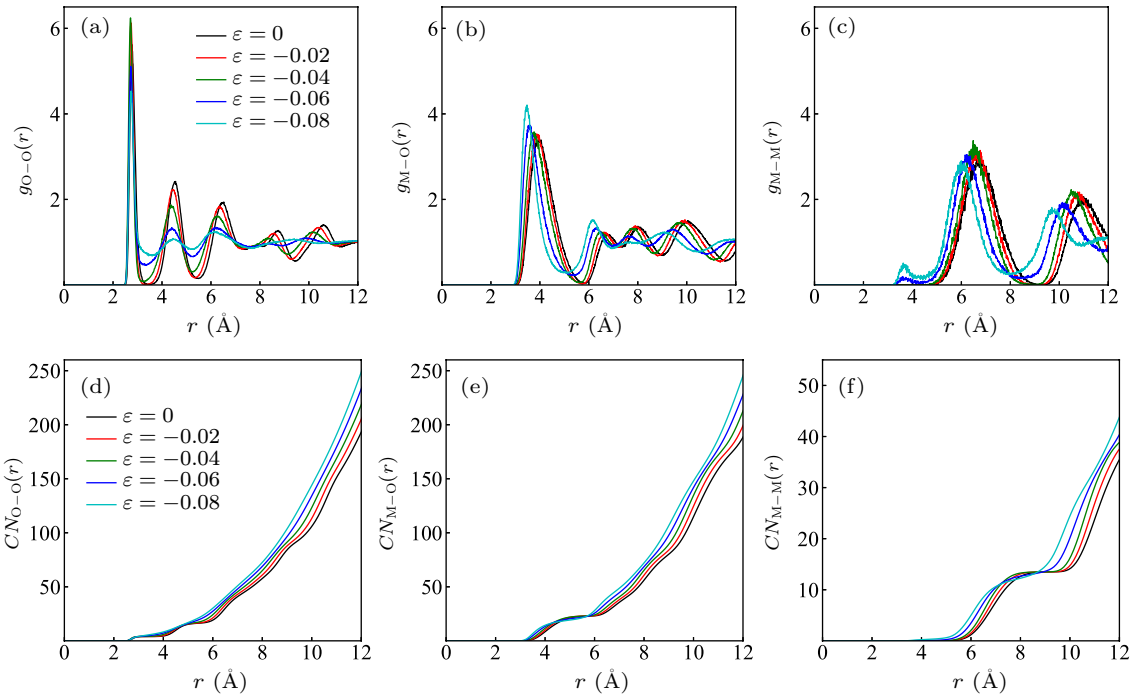


Fig. 6. (a)–(c) Radial distribution functions ($g(r)$) of oxygen–oxygen (O–O) pairs, methane–oxygen (M–O) pairs, and methane–methane (M–M) pairs in methane hydrate at strains of 0.00, −0.02, −0.04, −0.06, and −0.08. (d)–(f) Coordination number (*CN*) of O–O, M–O, and M–M pairs in methane hydrate at strains of 0.00, −0.02, −0.04, −0.06, and −0.08.

To quantitatively assess the order degree of the methane hydrate structure, we calculated the $F_{4\varphi}$ of water molecules:[44,45]

$$F_{4\varphi} = \frac{1}{n}\sum_{i=1}^{n}\cos(3\varphi_i), \tag{12}$$

where n represents the number of water molecules within a 0.35 nm radius around a given water molecule, and φ_i represents the ith angle between the oxygen atoms and the outermost hydrogen atoms. Different values of $F_{4\varphi}$ correspond to various phases of water: −0.04 for liquid water, −0.4 for solid ice, and 0.7 for solid hydrate. As illustrated in Fig. 7(a), we first calculated the $F_{4\varphi}$ of methane hydrate during the triaxial compression process. The results showed that $F_{4\varphi}$ decreased slowly from a strain of 0.00 to −0.04; however, when the strain exceeded −0.04, the value of $F_{4\varphi}$ decreased rapidly. This finding indicates that a triaxial strain of −0.04 serves as a threshold for the stability of methane hydrate. Furthermore, we employed the HTR package[46] to count the number of 5^{12} and $5^{12}6^2$ cages during triaxial compression. It was observed that the number of both types of hydrate cages vanished almost simultaneously at a strain of approximately −0.07. This demonstrates that there were almost no intact hydrate cages among the visualized residual hydrate cages at a

strain of −0.08, as depicted in Fig. 5(c). Additionally, nearly half of the cages in the hydrate were incomplete at a strain of −0.04. At this stage, the hydrate cage reached its critical yield stress point, and any additional increase in stress caused the hydrate cage to destabilize and rapidly disintegrate. However, within the ideal conditions (NVT and NVE) in this study, the residual hydrate structure can maintain its stability under this level of strain. For instance, we calculated the $F_{4\varphi}$ of methane hydrate during the EMD simulations. As shown in Fig. 7(b), the $F_{4\varphi}$ of methane hydrate under different compressive strains consistently fluctuated within a fixed range during the 1.5 ns microcanonical ensemble simulation process. This suggests that the residual hydrate structure remained stable during the EMD simulations. In this stable scenario, the movement of free water and methane within the hydrate structure may also influence the heat transport properties.

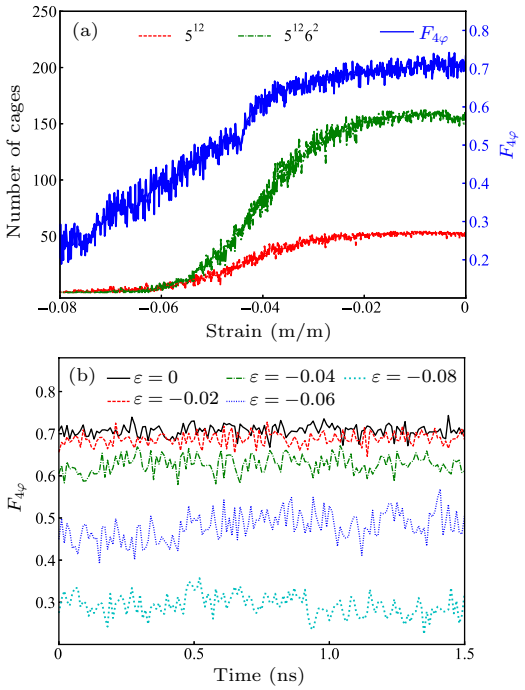


Fig. 7. (a) Number of cages and four-body angular order parameter ($F_{4\varphi}$) of the methane hydrate during the compression process. (b) $F_{4\varphi}$ of methane hydrate during the equilibrium molecular dynamics simulation processes at strains of 0.00, −0.02, −0.04, −0.06, and −0.08.

3.2.2. Diffusion properties

To investigate the mass transfer mechanism within the residual hydrate under different strains, we calculated the MSDs of methane and water molecules using

$$\mathrm{MSD}(t) = \left\langle |\boldsymbol{r}_i(t) - \boldsymbol{r}_i(0)|^2 \right\rangle, \tag{13}$$

where t is the simulation time, and $\boldsymbol{r}(t)$ and $\boldsymbol{r}(0)$ represent the positions of molecule i at time t and 0, respectively. Further, the self-diffusion coefficients (D_i) of methane and water molecules were computed using

$$D_i = \frac{1}{6}\lim_{t\to\infty}\frac{\mathrm{d}}{\mathrm{d}t}\sum_{i=1}^{N}\mathrm{MSD}(t), \tag{14}$$

where N represents the number of molecules. As shown in Fig. 8(a), we initially calculated the MSDs and D_i of methane and water within the hydrate during the compression process. In this process, we observed that the diffusion behavior of water molecules can be divided into three stages: A (8.5×10^{-11} m^2/s), B (6.4×10^{-11} m^2/s), and C (10.6×10^{-11} m^2/s). These findings suggest that when the strain is low (0.00 to −0.02), the water molecules have more room for compression, and the low resistance to compression leads to a high diffusion coefficient. As the strain increased from −0.02 to −0.04, the compression space available to the water molecules decreased, constraining their diffusion ability. Nevertheless, the structural stability of the local water cages decreased when the strain exceeded −0.04, resulting in a significant increase in diffusion capacity. Moreover, the diffusion capacity of the methane molecules was significantly lower than that of the water molecules, and its diffusion behavior can be divided into two stages: D (0.5×10^{-11} m^2/s) and E (1.26×10^{-11} m^2/s). Specifically, the low diffusion coefficient in the D stage may be primarily due to the methane molecules in the edge cages of the hydrate remaining stable as they moved toward the center under triaxial compressive strains. The diffusion capacity of the methane molecules in the central cages was lower than that of the methane molecules in the edge cages. However, methane gradually escaped from the hydrate cages at the edge (as depicted in Fig. 5(d)), sharply increasing its overall diffusion capacity during the E stage. Thus, the diffusion mechanism of methane molecules can be divided into two stages. Initially, only methane molecules within cages at the edges occurred at low strains (0.00 to −0.04), resulting in a low diffusion capacity. In the second stage, at large strains (−0.04 to −0.08), some methane molecules escaped as a result of the decomposition of local hydrates, which led to an increase in the diffusion coefficient.

Furthermore, the diffusion properties of water and methane molecules were calculated during the EMD simulation processes. As illustrated in Fig. 8(b), the MSD of the water molecules was nearly zero at strains of 0.00 and −0.02. However, the MSD of the water molecules significantly increased as the compressive strain increased. However, when the strain reached −0.06, the MSD of the water molecules reached the maximum and then decreased at a strain of −0.08. This reduction may have resulted from the smaller volume caused by strain, which restricted the diffusion range of the water molecules. Methane molecules exhibited a similar behavior, with their diffusion ability decreasing under a strain of −0.08, as depicted in Fig. 8(c). In addition, the MSD of methane molecules during the EMD process was approximately an order of magnitude lower than that of water molecules. The MSD of the methane molecules remained nearly constant at strains of 0.00, −0.02, and −0.04. Addi-

tionally, the initial values of MSD were dependent on the level of strain. The greater the compressive strain, the lower the initial MSD. This initial MSD value represents the diffusible range of methane molecules within the hydrate cage. As depicted in Fig. 8(d), we further calculated the D_i of methane and water molecules under various strains by fitting the MSD. The results indicate that water molecules dominated the mass transfer behavior in the residual methane hydrate. Moreover, the phonon transport analysis suggests that water molecules served as the primary medium for heat conduction. Therefore, the increased diffusion of water molecules may further enhance the thermal conductivity of methane hydrate. Additionally, the D_i values of both water and methane were almost zero at strains of 0.00 and −0.02. At a strain of −0.06, the D_i values of water and methane reached their peaks, but they decreased when the strain was at −0.08. The findings on residual hydrate stability suggest that most water cages were incomplete at a strain of −0.06, whereas there were almost no intact hydrate cages at a strain of −0.08. This indicates that more methane and water molecules were released at a strain of −0.08; however, their diffusion capacities were diminished. Based on the MSD results, we suspect that this may be due to the restricted activity space of the water molecules resulting from the reduction in volume. This compression increases the probability of collisions between atoms, which may also enhance heat transport. Therefore, methane hydrate is affected by the synergistic effect of higher diffusivity and increased collision rates in the unstable state. This explains the accelerated increase in the thermal conductivity of methane hydrate at higher compressions.

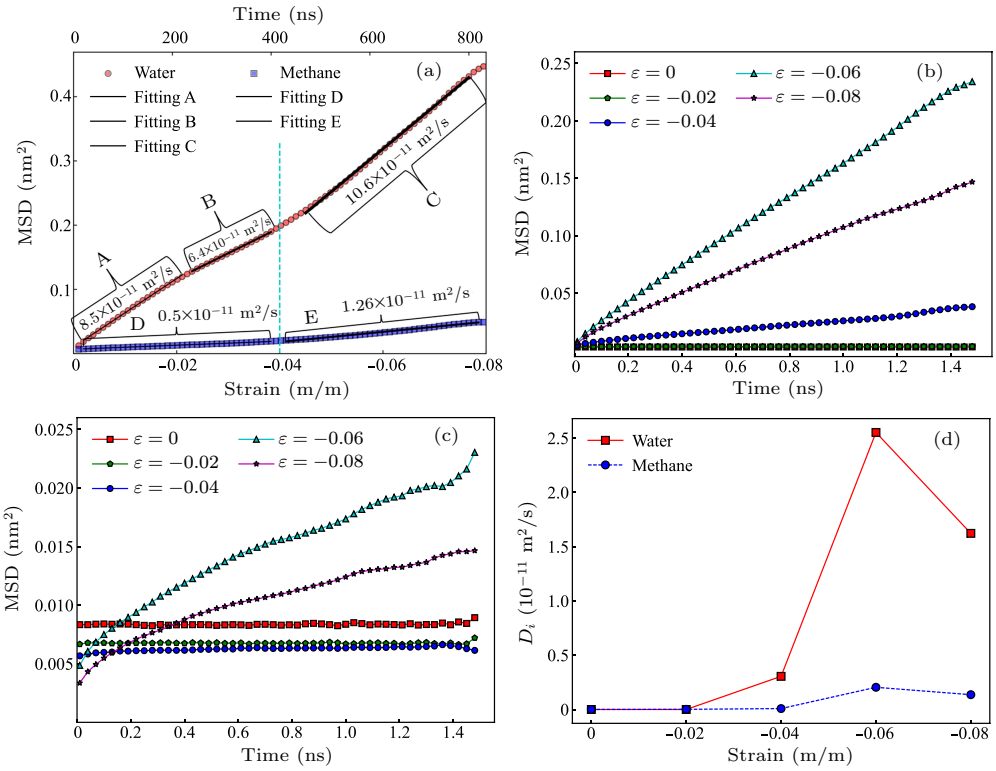


Fig. 8. (a) MSDs and diffusion coefficients (D_i) of water and methane molecules in the hydrate during the compression process. MSDs of (b) water and (c) methane molecules during the EMD processes at strains of 0.00, −0.02, −0.04, −0.06, and −0.08. (d) D_i of water and methane molecules obtained by fitting the MSDs in (b) and (c).

4. Conclusion and perspectives

In summary, we investigated the mechanisms of thermal transport and structural stability in sI-type methane hydrate under triaxial compressive strains using MD simulations. The results suggest that the thermal conductivity increases with an increase in the compressive strain. In particular, the rate of increase in thermal conductivity was faster in the strain range of −0.04 to −0.08 than in the range of 0.00 to −0.04. The PDOS and SED results demonstrate the overlap of vibration peaks between methane and water molecules at low frequencies in the strain range of 0.00 to −0.04, establishing a low-frequency phonon transport channel. In addition, the main peak valleys of the phonon vibration over the entire frequency range were almost filled when the triaxial compressive strain exceeded 0.04. These fillings facilitate the opening of more phonon transport channels. In terms of structural stability, we found that a strain of −0.04 serves as a critical transition point where methane hydrate changes from stable to unstable. Moreover, the results revealed that a strain of −0.06 was the point at which the diffusion capacities of methane and water molecules reached their maximum. At a higher strain (−0.08), the greater volume compression reduced the available space, thereby restricting the diffusion ability of the wa-

ter and methane molecules within the hydrate. The synergistic effect of the strong diffusion ability and high probability of collision between atoms increased the thermal conductivity of hydrates during the unstable period compared to the stable period. Therefore, it can be inferred that the high mass transfer capability resulting from the structural instability may account for the opening of more phonon transport channels. Our results offer valuable theoretical insights into the thermal conductivity and stability of methane hydrates in reservoir stress environments.

Given that most hydrates are situated within the porous medium of reservoirs, understanding the heat transfer properties between methane hydrates and the surrounding wall surface is essential for accurately predicting the overall heat transfer in the reservoir. The presence of a water layer and a gas layer between the methane hydrate and the wall introduces complexities to the interfacial heat transfer. This aspect will be the focus of future research.

Acknowledgement

Project supported by the National Natural Science Foundation of China (Grant Nos. 52376083 and 51991362).

References

[1] Sloan E D 2003 *Nature* **426** 353
[2] Ye J, Qin X, Xie W, Lu H, Ma B, Qiu H, Liang J, Lu J, Kuang Z, Lu C, Liang Q, Wei S, Yu Y, Liu C, Li B, Shen K, Shi H, Lu Q, Li J, Kou B, Song G, Li B, Zhang H, Lu H, Ma C, Dong Y and Bian H 2020 *China Geol.* **3** 197
[3] Chibura P E, Zhang W, Luo A and Wang J 2022 *J. Nat. Gas Sci. Eng.* **100** 104441
[4] Yu Y S, Zhang X, Liu J W, Lee Y and Li X S 2021 *Energy Environ. Sci.* **14** 5611
[5] Makogon Y F, Holditch S A and Makogon T Y 2007 *J. Pet. Sci. Eng.* **56** 14
[6] Liang Y, Tan Y, Luo Y, Zhang Y and Li B 2020 *J. Cleaner Prod.* **261** 121061
[7] Song B, Cheng Y, Yan C, Lyu Y, Wei J, Ding J and Li Y 2019 *J. Nat. Gas Sci. Eng.* **65** 197
[8] Chen C, Zhang Y, Li X S, Li G and Chen Z Y 2024 *Energy Fuels* **38** 5928
[9] Guo P, Pan Y K, Li L L and Tang B 2017 *Chin. Phys. B* **26** 073101
[10] Cortes D D, Martin A I, Yun T S, Francisca F M, Santamarina J C and Ruppel C 2009 *J. Geophys. Res. Solid Earth* **114** B1103
[11] Kim Y J and Yun T S 2013 *Mar. Pet. Geol.* **47** 77
[12] Morita H, Muraoka M and Yamamoto Y 2019 *Int. J. Offshore Polar Eng.* **29** 104
[13] Lei G, Tang J, Zhang L, Wu Q and Li J 2024 *Energy* **288** 129704
[14] Xu K, Lin Y, Shi Q, Li T, Zhang Z and Wu J 2022 *Phys. Chem. Chem. Phys.* **24** 5479
[15] Chen D, Miao T, Chang C, Guo X and Ji Z 2024 *Int. J. Heat Mass Transfer* **225** 125399
[16] Shu J, Chen X, Chou I M, Yang W, Hu J, Hemley R J and Mao H 2011 *Geosci. Front.* **2** 93
[17] Cao P, Wu J, Zhang Z, Fang B and Ning F 2018 *J. Phys. Chem. C* **122** 29081
[18] Lin Y, Liu Y, Xu K, Li T, Zhang Z and Wu J 2022 *Adv. Geo-Energy Res.* **6** 23
[19] Liu J, Fu R, Lin Y, Shi Q, Liu Y, Li T, Zhang Z and Wu J 2022 *ACS Sustainable Chem. Eng.* **10** 10339
[20] Zhang Y, Song Z, Lin Y, Shi Q, Hao Y, Fu Y, Wu J and Zhang Z 2024 *J. Phys.: Condens. Matter* **36** 015101
[21] Wang P, Wang J, Xu K, Lin Y, Shi Q, Li T, Fu Y, Zhang Z and Wu J 2022 *J. Mol. Liq.* **360** 119553
[22] Song Z, Zhou Z, Lin Y, Shi Q, Hao Y, Fu Y, Zhang Z and Wu J 2023 *Chin. Phys. B* **32** 066602
[23] Sloan E D 2003 *Nature* **426** 353
[24] Yousuf M, Qadri S B, Knies D L, Grabowski K S, Coffin R B and Pohlman J W 2004 *Appl. Phys. A* **78** 925
[25] Jewett A I, Stelter D, Lambert J, Saladi S M, Roscioni O M, Ricci M, Autin L, Maritan M, Bashusqeh S M, Keyes T, Dame R T, Shea J E, Jensen G J and Goodsell D S 2021 *J. Mol. Biol.* **433** 166841
[26] Stukowski A 2010 *Modell. Simul. Mater. Sci. Eng.* **18** 015012
[27] Abascal J L F, Sanz E, García Fernández R and Vega C 2005 *J. Chem. Phys.* **122** 234511
[28] Martin M G and Siepmann J I 1998 *J. Phys. Chem. B* **102** 2569
[29] Bernal J D and Fowler R H 1933 *J. Chem. Phys.* **1** 515
[30] Thompson A P, Aktulga H M, Berger R, Bolintineanu D S, Brown W M, Crozier P S, In 't Veld P J, Kohlmeyer A, Moore S G, Nguyen T D, Shan R, Stevens M J, Tranchida J, Trott C and Plimpton S J 2022 *Comput. Phys. Commun.* **271** 108171
[31] Luty B A and Van Gunsteren W F 1996 *J. Phys. Chem.* **100** 2581
[32] Ryckaert J P, Ciccotti G and Berendsen H J C 1977 *J. Comput. Phys.* **23** 327
[33] Evans D J and Holian B L 1985 *J. Chem. Phys.* **83** 4069
[34] Wang R, Liao B, Wang J, Sun J, Wang Y, Wang J, Wang Q, Qu Y and Cheng R 2023 *Chem. Eng. J.* **451** 138757
[35] Vogelsang R and Hoheisel C 1987 *Phys. Rev. A* **35** 3487
[36] An M, Wang H, Yuan Y, Chen D, Ma W, Sharshir S W, Zheng Z, Zhao Y and Zhang X 2022 *Surf. Interfaces* **28** 101690
[37] Thomas J A, Turney J E, Iutzi R M, Amon C H and McGaughey A J H 2010 *Phys. Rev. B* **81** 081411
[38] Miao T, Xiang M, Chen D, An M and Ma W 2022 *Int. J. Heat Mass Transfer* **183** 122099
[39] Ma D, Wan X and Yang N 2018 *Phys. Rev. B* **98** 245420
[40] Liu H and Paddison S J 2016 *Phys. Chem. Chem. Phys.* **18** 11000
[41] Ramasubramani V, Dice B D, Harper E S, Spellings M P, Anderson J A and Glotzer S C 2020 *Comput. Phys. Commun.* **254** 107275
[42] Humphrey W, Dalke A and Schulten K 1996 *J. Mol. Graph.* **14** 33
[43] Tian S, Wu T, Hu S, Ma D and Zhang L 2024 *Appl. Phys. Lett.* **124** 042202
[44] Rodger P M, Forester T R and Smith W 1996 *Fluid Phase Equilib.* **116** 326
[45] Wang Z, Yang L, Liu C and Lin S 2023 *Chin. Phys. B* **32** 023101
[46] Liu Y, Xu K, Xu Y, Liu J, Wu J and Zhang Z 2022 *Nanotechnol. Rev.* **11** 699